Journal of Materials Chemistry A

PAPER

View Article Online
View Journal | View Issue

Cite this: J. Mater. Chem. A, 2017, 5, 14422

Dual carbon layer hybridized mesoporous tin hollow spheres for fast-rechargeable and highly-stable lithium-ion battery anodes†

Weili An,[a] Jijiang Fu,[a] Shixiong Mei,[a] Lu Xia,[a] Xingxing Li,[a] Huazhi Gu,[a] Xuming Zhang,*[ab] Biao Gao,*[a] Paul K. Chu[b] and Kaifu Huo[c]

Received 15th February 2017
Accepted 13th June 2017

DOI: 10.1039/c7ta01399j

rsc.li/materials-a

Although tin-based nanocomposites are potential fast-charging anode materials for lithium-ion batteries to replace graphite-based materials due to their high theoretical capacity, they have some practical limitations such as relatively poor cycle stability which is caused by the large volume change and aggregation of Sn. Herein, we report a conjoined Sn/C hollow spherical nanocomposite (MSHSs@C/C) prepared by double DA polymerization and annealing. MSHSs@C/C with ultrasmall Sn nanoparticles (5–8 nm) embedded in its conductive carbon matrix can achieve a large Sn mass loading of 75% and overcome the aggregation and volumetric expansion of Sn during cycling. The MSHSs@C/C anode delivers an excellent performance including a high reversible capacity of 831 mA h g^{-1} at a current density of 0.1 A g^{-1}, a capacity retention of 42.5% when the density is increased 100 times from 0.1 to 10 A g^{-1}, a capacity of 325 mA h g^{-1} at a large current density of 10.0 A g^{-1} (10C, 1C = 1.0 A g^{-1}) after 4000 cycles, and superior cycling stability. Fast charging can be accomplished in 2.5 min and the MSHSs@C/C anode overcomes many of the intrinsic problems plaguing Sn-based anode materials in Li-ion batteries.

Introduction

Lithium-ion batteries (LIBs) have attracted increasing attention in energy storage due to their superior energy density, operating voltage and cycle life.[1,2] However, the charging times of commercial LIBs range from 1 to 2 h due to the sluggish electron transfer kinetics and Li ion diffusion in the anode and cathode.[3] The energy density of commercial LIBs decreases severely at large charging rates, which causes problems for electric vehicles. To be competitive with gas driven cars, the LIB in an electric vehicle should have a fast charging performance at a charging rate of 10C (discharging in 6 min).[3] Fast-charging anodes such as intercalated oxides, alloys, and conversion oxides with high capacity and stability have been proposed to replace the graphite anode (372 mA h g^{-1}).[4–6] In particular, tin (Sn) has been investigated extensively due to its high theoretical capacity (994 mA h g^{-1}), abundance, and environmental friendliness.[4,7] Nevertheless, the practical implementation of Sn anodes in LIBs is hampered by poor cycling as a result of the substantial volume change (260%) and low rate performance in the lithiation/delithiation process.[8–11] Sn nanostructures have been shown to mitigate the volume change and mechanical stress during the alloying/dealloying process because of their large surface/volume ratios.[12–14] However, the aggregation of Sn nanostructures is still inevitable which adversely affects cycling.[12,15–19] A solution to this is to design hybrid materials in which Sn is uniformly dispersed in a conductive matrix on the nanoscale in order to minimize aggregation and buffer the volumetric expansion of the electrode[20,21] Carbon-based materials with a large specific area and considerable conductivity such as carbon nanotubes, graphene, and carbon nanofibers have been combined with Sn nanostructures to improve the Li storage performance.[22–28] Yu *et al.* reported that carbon microtubes encapsulated with Sn particles exhibited a reversible capacity of 737 mA h g^{-1} at 0.25 A g^{-1} after 200 cycles[26] and Wang *et al.* fabricated a nano-Sn/C hybrid with ultrafine Sn (10 nm) uniformly dispersed in spherical carbon *via* aerosol spray pyrolysis.[27] Meschini *et al.* demonstrated that an Sn@C nanocomposite prepared *via* co-electrospinning achieved considerable stability with a capacity of 350 mA h g^{-1} after 600 cycles at 1 A g^{-1}.[28] Most Sn/C composites are synthesized by externally injecting the SnO_2 precursor into a carbon frame and then reduced by annealing which may lead to a small Sn mass loading (less than 60%). Moreover, poor homogeneity and grain growth during annealing due to the low melting point of metallic Sn (232 °C) limit their electrochemical

[a]The State Key Laboratory of Refractories and Metallurgy, Wuhan University of Science and Technology, Wuhan 430081, China. E-mail: gaobiao@wust.edu.cn; xumzhang@wust.edu.cn; guhuazhi@163.com; Tel: +86-13517240510

[b]Department of Physics and Materials Science, City University of Hong Kong, Tat Chee Avenue, Kowloon, Hong Kong, China

[c]Wuhan National Laboratory for Optoelectronics (WNLO), School of Optical and Electronic Information, Huazhong University of Science and Technology, Wuhan 430074, China

† Electronic supplementary information (ESI) available. See DOI: 10.1039/c7ta01399j

performance.[28,29] Thus, it is still challenging to produce fast-charging highly-stable Sn/C nanocomposites with a large mass loading.

In this work, conjoined hollow Sn/C spheres (MSHSs@C/C) are fabricated *via* dopamine hydrochloride (DA) two-step polymerization on mesoporous hollow SnO_2 spheres ($MHSnO_2$) and annealing in Ar/H_2. Scheme 1 depicts the synthetic process of MSHSs@C and MSHSs@C/C. $MHSnO_2$ consisting of the ultrafine nanoparticles is fabricated *via* a hydrothermal method. Subsequently, $MHSnO_2$ is conformally coated and uniformly embedded by polydopamine ($MHSnO_2$@PDA) in the first DA chemical polymerization. Then, $MHSnO_2$@PDA is interconnected with each other *via* a second DA polymerization step to form the dual PDA coated $MHSnO_2$ dual PDA composite ($MHSnO_2$@PDA/PDA). Finally, the dual PDA-derived carbon composited Sn hybrid is obtained *via* a reduction annealing process. MSHSs@C/C is promising as an ideal fast recharging lithium ion battery anode owning to following advantages. First, the ultrasmall Sn nanoparticles (5–8 nm) distributed uniformly in the carbon matrix balance the conflict between high mass loading (75%) and high activity of nano-Sn, which contributes to the outstanding reversible capacity of the Sn/C composite. Then, Sn nanoparticles can be isolated by the three dimensional (3D) and conformal carbon on their surface, which can endure much higher mechanical stress and mitigate pulverization. Moreover, the MSHSs@C hollow spheres are further integrated by the outer layer carbon network derived from secondary DA polymerization, which decreases the contact resistance between particles and improves the integrity of the electrode materials even at a large rate. As an anode in LIBs, MSHSs@C/C has a high reversible capacity of 831 mA h g^{-1} (84% of the theoretical capacity) at a current density of 0.1 A g^{-1}, a capacity retention of 42.5% when the density is increased 100 times from 0.1 to 10 A g^{-1}, and a high reversible capacity of 616 mA h g^{-1} at 1.0 A g^{-1} with no obvious capacity decay after 1000 cycles. Even at a large current density of 10.0 A g^{-1}, MSHSs@C/C retains a capacity of 325 mA h g^{-1} after 4000 cycles. The 3D Sn/C composite is suitable for fast-recharging LIBs and can be extended to other high-capacity anode materials such as silicon and germanium.

Experimental

Sample preparation

In a typical synthesis, 0.275 g of urea (Aladdin, 99%) was dissolved in an ethanol (20 mL) and water (35 mL) mixed solution and 0.264 g of potassium stannate trihydrate ($K_2SnO_3 \cdot 3H_2O$, Aladdin, 99.9%) was added slowly under stirring for 30 minutes to obtain a translucent solution. The solution was transferred to an 80 mL Teflon-lined stainless steel autoclave and heated to 200 °C for 20 h in an electric oven. After washing and centrifuging with deionized water several times, the white product was collected by freeze-drying for 24 h.

$MHSnO_2$@PDA was prepared *via* a DA polymerization method. Typically, 0.25 g of $MHSnO_2$ was dispersed in 200 mL of distilled water containing 0.28 g of 2-amino-2-hydroxymethyl-propane-1,3-diol (Tris, Sigma-Aldrich, 98%) under stirring. Subsequently, 0.6 g of DA (Aladdin, 98%) was added and stirred at room temperature (25 °C) for 6 h in air. $MHSnO_2$@PDA was obtained after washing with distilled water three times. Then, $MHSnO_2$@PDA/PDA was obtained *via* a DA polymerization process on $MHSnO_2$@PDA. Similarly to the above procedure, 0.2 g of $MHSnO_2$@PDA was dispersed in 200 mL deionized water containing Tris (0.24 g) and 0.24 g of DA. The reaction was conducted for 1 h under stirring to produce $MHSnO_2$@PDA/PDA. For comparison, we coated $MHSnO_2$ with a PDA layer in one step using double the amount of dopamine hydrochloride, which was denoted as $MHSnO_2$@PDA-2.

Both MSHSs@C and MSHSs@C/C were obtained by annealing $MHSnO_2$@PDA and $MHSnO_2$@PDA/PDA at 400 °C for 1 h and then at 650 °C for 4 h in an Ar/H_2 (95 : 5 vol/vol) atmosphere at a heating rate of 3 °C min^{-1}. The control sample of mesoporous Sn hollow spheres (MSHSs) was prepared by annealing $MHSnO_2$ in an Ar/H_2 atmosphere. The

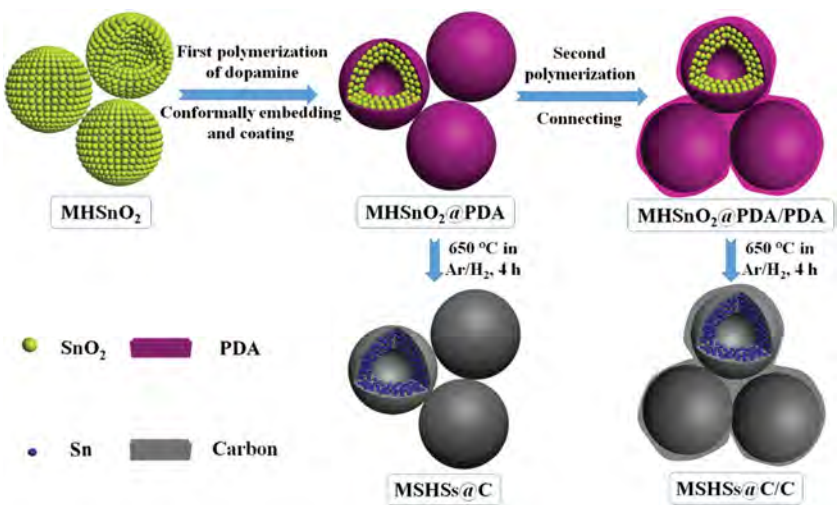

Scheme 1 Schematic illustration of the fabrication procedures of MSHSs@C and MSHSs@C/C.

Sn/C composite obtained by annealing $MHSnO_2$@PDA-2 was denoted as MSHSs@C-2.

Material characterization

The morphology, structure, and composition of the samples were characterized *via* field-emission scanning electron microscopy (FE-SEM, FEI Nano 450), transmission electron microscopy (TEM, FEI Tecnai G20), X-ray diffraction (XRD, Philips X'Pert Pro), X-ray photoelectron spectroscopy (XPS, ESCALab 250), and Raman scattering (HB RamLab). The C content in MSHSs@C/C was determined *via* thermogravimetry/differential scanning calorimetry (TG/DSC, STA449/6/G NETZSCH) in the temperature range of 30 °C and 1000 °C at a rate of 5 °C min^{-1} in air atmosphere. Nitrogen adsorption and desorption isotherms were measured using the Brunauer–Emmett–Teller (BET) method on a surface area analyzer (Micrometrics, ASAP 2020) after degassing the samples at 453 K for 8 h.

Electrochemical measurements

Electrodes were fabricated by spreading a slurry on Cu foil. The slurry was obtained by mixing the active materials, sodium alginate, and carbon black at a ratio of 7 : 2 : 1 which was then pasted on copper current collectors using an automatic thick film coater (MTI, MSK-AFA-III). The area mass loading of the active material on the electrode was 0.71–0.86 mg cm^{-2}. After drying under vacuum at 80 °C overnight, CR2016 type coin cells were assembled in a glove box (Vigor SG1200/750TS-C) with a Celgard 2400 film separator and pure Li foil counter electrode. The electrolyte was 1 M $LiPF_6$ in a 1 : 1 (volume) mixture of ethylene carbonate and diethyl carbonate with 6% vinylene carbonate. Cyclic voltammetry (CV) was performed on an electrochemical workstation (CHI 760e) in the potential window from 0.01 to 3.0 V (*vs.* Li/Li^+). Electrochemical impedance spectroscopy (EIS) was carried out on the CHI 760e in the frequency range of 100 kHz to 0.01 Hz at an amplitude of 5 mV. The assembled coin cells were cycled galvanostatically on a battery tester (LAND, CT2001A) in the voltage range between 0.01 and 3.0 V.

Results and discussion

The SEM and TEM images of the hydrothermal product in Fig. S1a and S2a and b (ESI†) show that $MHSnO_2$ has a hollow spherical morphology with a shell thickness of 30–40 nm and diameter of about 220 nm (inset in Fig. S1a, ESI†) and the XRD peaks correspond to tetragonal SnO_2 (Fig. S1b, ESI†). The TEM images (Fig. S2a and b, ESI†) show that the porous SnO_2 nanosphere consists of small nanoparticles with a diameter of 5–8 nm. The parallel fringes with the spacing of 0.35 nm in the HR-TEM image (inset in Fig. S2b, ESI†) correspond to the (110) plane of crystalline tetragonal SnO_2. The nitrogen adsorption–desorption isotherms (Fig. S5a, ESI†) of $MHSnO_2$ show an obvious hysteresis loop, which indicates a mesoporous structure. The specific surface area measured by the Brunauer–Emmett–Teller (BET) method is 77.8 m^2 g^{-1} and the pore-size distribution is in the range of 5 to 8 nm, which was obtained by the Barrett–Joyner–Halenda (BJH) method. The porous structure of the SnO_2 nanospheres results from the stacking of the small SnO_2 nanoparticles in the shell. After the first DA polymerization process, $MHSnO_2$@PDA retains the dispersed spherical morphology. $MHSnO_2$ was coated by an amorphous layer with the thickness of 35 nm and most of the nanopores in $MHSnO_2$ are not obvious, as shown in Fig. S2c and d (ESI†), which indicates that PDA is embedded in the pores of $MHSnO_2$. After annealing $MHSnO_2$@PDA in Ar/H_2, the dispersed MSHSs@C (Fig. 1a) with a smooth surface similar to $MHSnO_2$@PDA was obtained. Fig. 1b shows the SEM image of MSHSs@C/C obtained by annealing $MHSnO_2$@PDA/PDA (Fig. S2e and f, ESI†) which reveals that MSHSs@C is interconnected by a 3D continuous carbon network derived from the secondary polymerization of DA. The TEM image in Fig. S3a (ESI†) shows that the MSHSs@C/C hollow spheres with a diameter of 220 nm and thickness of 40 nm are connected to each other by the carbon framework and abundant Sn nanoparticles are embedded in the shell of the nanospheres, as shown in Fig. 1c and d. The typical size of the Sn nanoparticles is 5–8 nm, as shown in the HR-TEM image (Fig. S3b, ESI†). The inset in Fig. 1d shows a set of parallel fringes with spacing of 0.29 nm corresponding to the (101) plane of crystalline Sn, which is consistent with the SAED image (inset in Fig. S3b, ESI†).

The XRD peaks of MSHSs@C/C in Fig. 2a can be indexed to the pure tetragonal metallic Sn phase (JCPDS Card no. 04-0673) and no SnO_2 residue is found, which implies that SnO_2 was converted into Sn during the reduction process.[7,30,31] The XPS survey spectrum of MSHSs@C/C is depicted in Fig. 2b, which

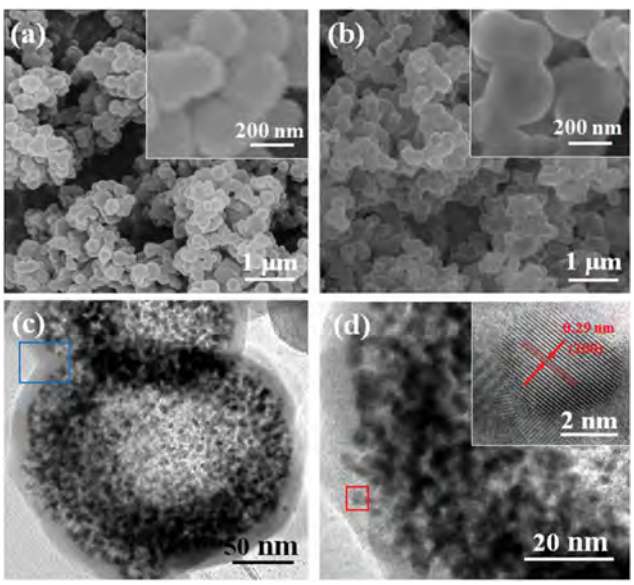

Fig. 1 SEM images of (a) MSHSs@C and (b) MSHSs@C/C nanospheres with the insets showing the corresponding magnified SEM images; (c) TEM image (blue region is the connection between the two MSHSs@C/C nanospheres) and (d) HR-TEM image of MSHSs@C/C, where the inset is a magnified image of the red square region.

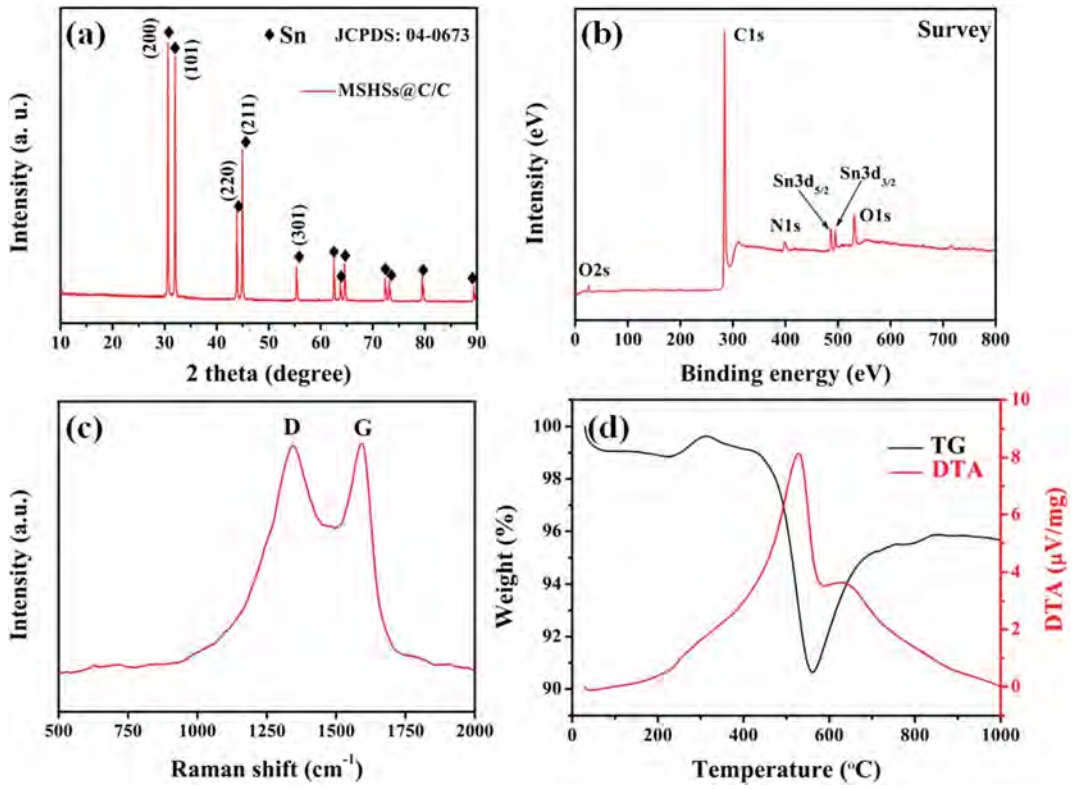

Fig. 2 (a) XRD pattern, (b) survey XPS spectrum, (c) Raman scattering spectrum, and (d) TG/DTA curves of MSHSs@C/C.

indicates that the sample contains C, N, O, Sn and N elements. The Sn 3d spectrum (Fig. S4a, ESI†) shows two characteristic peaks at 486.4 eV (Sn $3d_{5/2}$) and 494.9 eV (Sn $3d_{3/2}$) which are indicative of SnO_x. SnO_x is produced by the surface oxidization of metallic Sn[8,12] and it is confirmed by the high-resolution O 1s XPS spectrum in Fig. S4b.†[2] The two peaks at 484.7 eV (Sn $3d_{5/2}$) and 493.3 eV (Sn $3d_{3/2}$) result from metallic Sn. The high-resolution C 1s XPS spectrum (Fig. S4c†) can be divided into three peaks which correspond to C–C (284.6 eV), C═N (285.9 eV), and O═C–N (287.5 eV).[14] The high-resolution N 1s spectrum (Fig. S4d†) can be fitted with pyridinic N (398.4 eV), pyrrolic N (400.1 eV), graphite N (401.0 eV), and oxidized pyridinic N (403.1 eV), indicating that N is a dopant in the carbon matrix[32,33] which can enhance the electrical conductivity and wettability of the electrode.[12] The peaks at 1338 and 1590 cm^{-1} in the Raman spectrum of MSHSs@C/C in Fig. 2c can be assigned to the D and G bands of amorphous carbon, respectively.[32] Fig. 2d presents the TG and DTA plots of MSHSs@C/C between 30 °C and 1000 °C at a rate of 5 °C min^{-1} in air. The TG plot shows that the Sn content in MSHSs@C/C is as high as 75 wt%, which is higher than that in previously reported Sn/C composites.[11,12,24,26,34]

To determine the structure of the 3D interconnected carbon shell, MSHSs@C/C was dissolved in diluted HCl to remove the Sn nanoparticles. The SEM and TEM images in Fig. 3a and b indicate that the double-shell carbon hollow spheres (DCHSs) are interconnected with carbon resulting from the carbonization of PDA. The structure of the DCHSs revealed by HR-TEM (Fig. 3c) discloses that they consist of an inner shell (blue arrow) and outer shell (black arrow). The connection of the DCHSs (indicated in the red region) not only favors electron transfer between different spheres but also enhances the contact and structural stability of the Sn/C composite. Pores

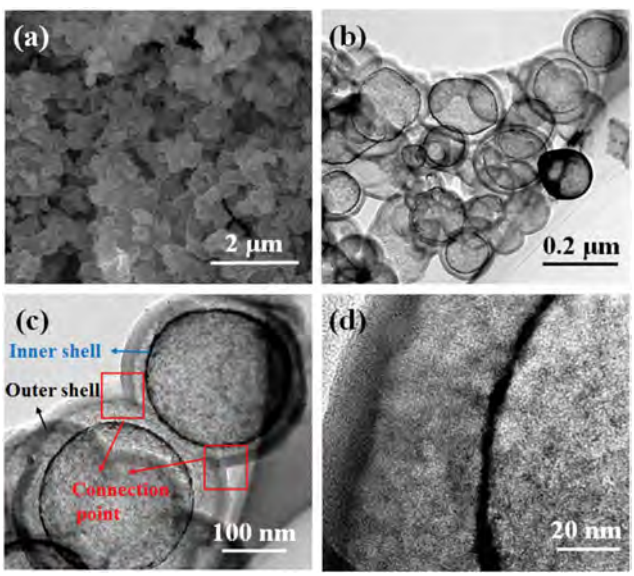

Fig. 3 (a) SEM images of the DCHSs after removing the Sn nanoparticles from MSHSs@C/C with HCl; (b and c) TEM images of DCHSs with the red region showing the connection points between two DCHSs and (d) HR-TEM image of the shell in the DCHSs.

with a size range of 5–8 nm are observed from the shell of the hollow spheres due to dissolution of the Sn nanoparticles. The N_2 adsorption–desorption isotherms are shown in Fig. S5 (ESI†). The BET specific surface areas of $MHSnO_2$, MSHSs@C, MSHSs@C/C, and DCHSs are 77.8, 161.6, 215.2, and 435.5 m^2 g^{-1}, respectively. The extra surface area of MSHSs@C and MSHSs@C/C compared to $MHSnO_2$ arises from the porous structure of the PDA-derived carbon and volume shrinkage due to the reduction of SnO_2 to Sn. MSHSs@C, MSHSs@C/C, and DCHSs show the typical mesoporous structure with pore size distributions of 2–3, 2–3, and 3–5 nm, respectively, according to the hysteresis loop in the N_2 adsorption–desorption isotherms and pore distribution plots.

The electrochemical properties of the samples were investigated in a half-cell with Li foil as the counter electrode. Fig. 4a shows the first five CV cycles of MSHSs@C/C at a scanning rate of 0.1 mV s^{-1} in the potential range from 0.01 to 3.0 V. During the first cathodic process, the irreversible broad peak at 1.2 V is associated with the formation of an SEI layer or irreversible reduction of SnO_2 on the surface of Sn.[4] The other two reduction peaks at 0.37 and 0.63 V arise from the lithiation of Sn with lithium ions to form Li–Sn alloys (Li_xSn_y), whereas the four oxidation peaks at 0.54, 0.62, 0.72, and 0.79 V in the oxidization process correspond to the extraction of lithium ions from the Li_xSn_y alloy phases ($Li_{22}Sn_5$ to Li_7Sn_3, LiSn, Li_2Sn_5, and Sn, respectively).[35] The oxidation peak at 1.18 V originates from the conversion of LiC_x to C.[36] The CV curves overlap quite well after the first cycle which is indicative of a reversible reaction on MSHSs@C/C. Fig. 4b shows the galvanostatic charging–discharging profiles of MSHSs@C/C at a current density of 0.05 A g^{-1} for the first cycle and the 1000th cycle at 1.0 A g^{-1}. The plateaus at 0.39 and 0.54 V during the alloying process are attributed to the formation of Li_xSn[7–10,17] and that at 0.54, 0.62, 0.72, and 0.79 V are ascribed to the dealloying character of Li_xSn which are in agreement with the CV curves. The initial lithiation and delithiation capacities at 0.05 A g^{-1} are 1250.4 and 999.5 mA h g^{-1}, respectively, which give a high initial coulombic efficiency of 80%. The initial capacity decay stems from the formation of an SEI layer[31–33] and irreversible insertion of Li^+ in the DCHSs.[34] After 1000 cycles, the galvanostatic charging–discharging curves of MSHSs@C/C almost overlap with a reversible capacity of 616 mA h g^{-1} which exhibits high cycling stability.

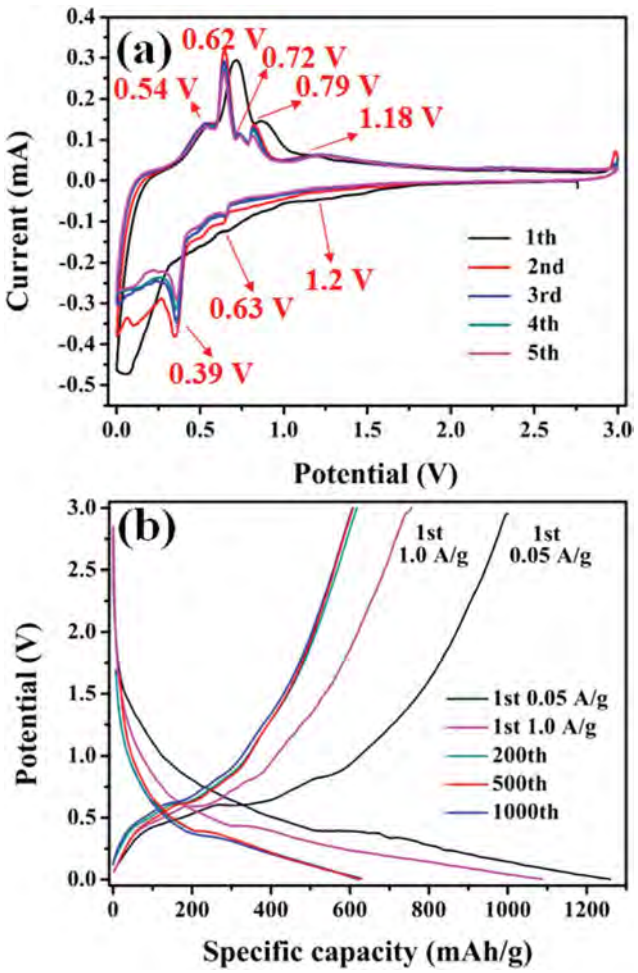

Fig. 4 (a) Typical CV curves of MSHSs@C/C at a potential sweep rate of 0.1 mV s^{-1} and (b) charging–discharging profiles of MSHSs@C/C at a current density of 1.0 A g^{-1}.

To obtain direct evidence of the enhanced Li ion storage performance of MSHSs@C/C, a comparison between MSHSs, MSHSs@C, and MSHSs@C/C is presented in Fig. 5, which shows the rate performance of MSHSs, MSHSs@C, and MSHSs@C/C at various current densities from 0.1 to 10 A g^{-1}. At a low current density of 0.1 A g^{-1}, MSHSs@C/C has a specific reversible capacity of 828 mA h g^{-1}. When the current density is increased 100 times from 0.1 to 10 A g^{-1}, MSHSs@C/C delivers a capacity of 352 mA h g^{-1} with a capacity retention of 42.5%. After the current density is returned to 0.1 A g^{-1}, a reversible and recoverable capacity of 826 mA h g^{-1} is obtained due to the excellent structural integrity of MSHSs@C/C. The rate performance of MSHSs@C/C is superior to that of the MSHSs electrode for the following reasons. First, carbon derived from the first DA polymerization process conformally encapsulates each Sn nanoparticle resulting in 3D channels for rapid electron transfer and lithium ion diffusion. Secondly, carbon connects each MSHSs@C to decrease the resistance between spheres. MSHSs@C/C also exhibits better recoverability during high-rate cycling than MSHSs and MSHSs@C due to its superior structural stability and integrity which facilitate fast electron transfer and ion diffusion. The rate performance comparison is summarized in Fig. 5b, which confirms the superior properties of MSHSs@C/C compared to that of previously reported Sn/C composites.[2,4,6,11,13,29,37–40] The superior rate capability of MSHSs@C/C arises from the compositing of the ultrasmall Sn nanoparticles and porous carbon matrix which results in a shorter ion diffusion distance and lower resistance during charging and discharging. Fig. 5c shows the Nyquist impedance plots of MSHSs, MSHSs@C, and MSHSs@C/C after 500 cycles in a fully charged state. The Nyquist plots can be fitted with four elements including the resistance of the electrolyte (R_Ω), Li ion migration resistance between the solid electrolyte interface (SEI) and electrolyte (R_{sf}), charge transfer resistance (R_{ct}), and Warburg impedance (Z_w) resulting from the diffusion resistance of lithium ions in the electrode. As shown in Table S1 (ESI†), the

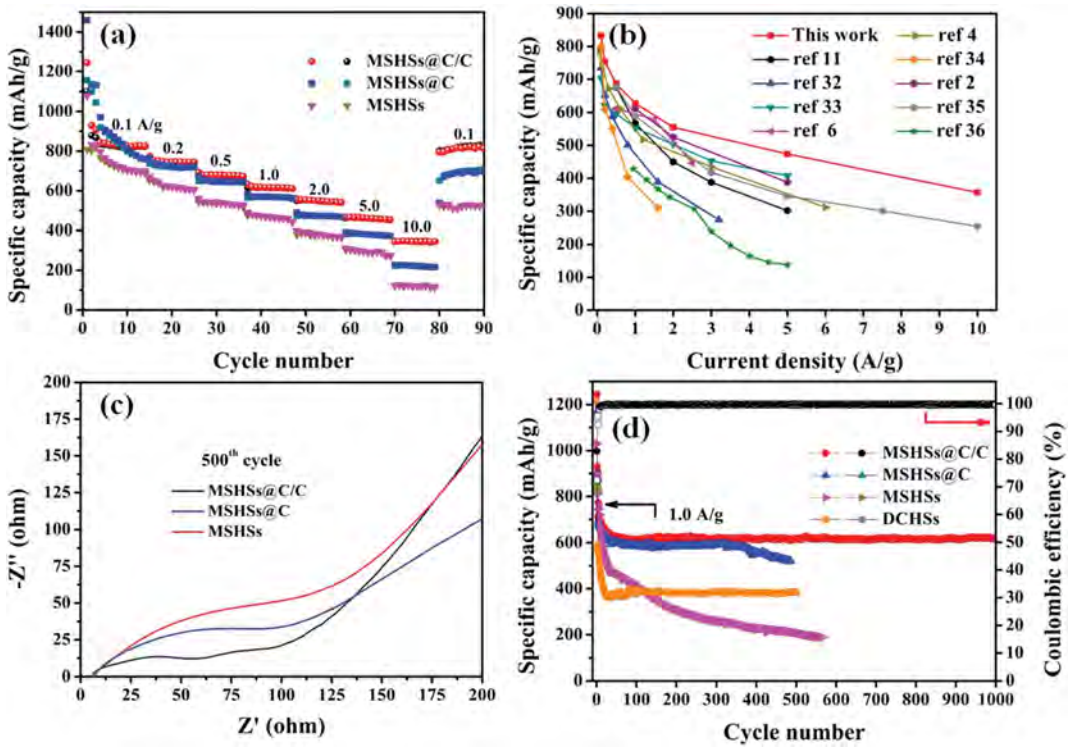

Fig. 5 (a) Capacity at different current densities; (b) rate capability comparison between MSHSs@C/C and previously reported Sn/C composites; (c) Nyquist plots of MSHSs, MSHSs@C, and MSHSs@C/C and (d) cycling performance of MSHSs, MSHSs@C, MSHSs@C/C, and DCHSs.

R_{ct} of MSHSs@C/C is 53.15 Ω which is smaller than that of MSHSs (139.3 Ω) and MSHSs@C (118.45 Ω). The smaller R_{ct} of MSHSs@C/C results from the stable SEI film, which gives rise to a better rate performance.

Fig. 5d shows the cycling performance of MSHSs, MSHSs@C, MSHSs@C/C and DCHSs at a current density of 1.0 A g^{-1}. MSHSs@C/C delivers superior cycle stability with a high reversible capacity of 616 mA h g^{-1} at 1.0 A g^{-1} and 81.6% capacity retention after 1000 cycles. To understand the tolerance of volume expansion of Sn upon full lithiation, the cyclic performance of MSHSs@C/C at a low current density of 0.2 A g^{-1} was tested, which showed a stable capacity of 790 mA h g^{-1} after about 150 cycles (Fig. S6a, ESI†). Moreover, we compared the thickness of the electrode films before and after 150 cycles in Fig. S6b and c.† The MSHSs@C/C electrode shows only ~20% volume expansion after 150 cycles at 0.2 A g^{-1}, which exhibits its excellent ability to relieve volume expansion. The DCHSs also showed a superior cycling stability with a stable reversible capacity of 383.1 mA h g^{-1} due to the nitrogen atom doping which is confirmed by the typical CV curves and charge–discharge profiles (Fig. S7a and b, ESI†).[41–43] The connected special hollow structures with nitrogen atom doping can work as electrochemical carriers for Sn NPs. Besides, the pure MSHSs (Fig. S8, ESI†) exhibit obvious capacity fading with a low capacity of about 194 mA h g^{-1} after 500 cycles. The poor stability of MSHSs is due to the electrochemical aggregation of Sn nanoparticles during the charging and discharging processes. The bare MSHSs collapse and agglomerate after 500 cycles (Fig. S9a, ESI†). MSHSs@C obtained by the one DA polymerization step followed by annealing shows high stability during the first 300 cycles, which is much better than that of the bare MSHSs. The improved cycle capability of MSHSs@C can be ascribed to the conformal carbon coating on the Sn nanoparticles which provide firm mechanical support to mitigate the effects of volume expansion in MSHSs@C and separates each Sn nanoparticle to avoid electrochemical agglomeration. To understand the effects of the carbon matrix in buffering the volume expansion of Sn at a large current density, we obtained an HR-TEM image (Fig. S9b†) of MSHSs@C after full lithiation in the 20th cycle at 1.0 A g^{-1}. The size of the Sn nanoparticles increased after full lithiation and they were still encapsulated in the carbon matrix. No obvious cracks are observed in the carbon shell matrix. However, obvious capacity decay is observed after 400 cycles from MSHSs@C due to the structural damage in the nanospheres resulting from repeated stress during charging/discharging. Although MSHSs@C retains its spherical morphology after 400 charging/discharging cycles at a large current density (Fig. S10a, ESI†), the Sn nanoparticles in MSHSs@C show huge outward volume expansion which can cause contact failure and destruction/regeneration of the SEI (Fig. S10b†). The R_{sf} values (Fig. S10c†) of MSHSs@C after 250 and 500 cycles are 21.28 and 40.87 Ω, respectively. The increase in R_{sf} reveals the instability of the SEI in MSHSs@C. MSHSs@C/C exhibits robust cycling stability without capacity decay even after 1000 cycles at 1.0 A g^{-1} and its performance is better than that of MSHSs@C. Besides, we coated $MHSnO_2$ with double the amount of DA ($MHSnO_2$@PDA-2) and then obtained MSHSs@C-2 after the same annealing process. The SEM and

TEM images (Fig. S11a–d†) of $MHSnO_2$@PDA-2 and MSHSs@C-2 indicate that the hollow spheres cannot be conjoined *via* one-step coating. The conjoined Sn/C hollow spheres can only be obtained *via* the two-step dopamine coating process, which will contribute to higher structural stability and enhanced conductivity. In addition, the Sn/C spheres obtained *via* the two-step coating method exhibit a more stable cycling performance and better rate capability than that of the one-step coating sample with double the amount of dopamine, as shown in Fig. S11e and f.†

EIS was conducted on the MSHSs@C/C electrode after the 1st, 200th, 500th, and 1000th cycles at a current density of 1.0 A g^{-1} (Fig. S12a, ESI†). The impedance parameters obtained from the modified equivalent circuit (Fig. S12b†) can be divided into R_Ω, two semicircles signaling Li^+ migration through the SEI (R_{sf}), and R_{ct}. The R_{sf} in Fig. S9a† decreases during the first 200 cycles due to the activation of the electrode materials and then is stable up to 1000 cycles, as shown in Table S2 (ESI†), due to the formation of a stable SEI film. The small rate variation in R_{ct} during cycling indicates a stable SEI film and structural stability of the nanocomposite which facilitate speedy charge transfer, faster kinetics in the electrochemical reactions, and a small polarization effect.[44] The carbon connecting each nanosphere can effectively avoid the contact failure of MSHSs@C. As shown in Fig. 6, the long-term cycling tests of MSHSs@C/C at a large current density demonstrate capacities of 616 mA h g^{-1} at 1.0 A g^{-1} after 1000 cycles, 464 mA h g^{-1} at 5.0 A g^{-1} after 2500 cycles, and 325 mA h g^{-1} at 10.0 A g^{-1} after 4000 cycles. The galvanostatic charging and discharging curves show a short discharging time of 2.5 min at a high rate (10C), as shown in the inset in Fig. 6.

The SEM and TEM images after 1000 cycles at 1.0 A g^{-1} (Fig. 7a and b, respectively) and 4000 cycles at 10 A g^{-1} (Fig. S13a and b, ESI,† respectively) reveal morphological changes. Sn nanoparticles with a diameter of 5–8 nm are uniformly embedded in the shell of the nanosphere (Fig. 6b and S13c†) after 1000 and 4000 cycles which confirms that the dual carbon matrix can effectively prevent the aggregation of Sn nanoparticles and ensure the integrity of the composite. The excellent electrochemical properties arise from the synergistic effects rendered by the 3D porous interconnected carbon network derived from the double polymerization of DA and uniform dispersion of ultrasmall Sn nanoparticles.

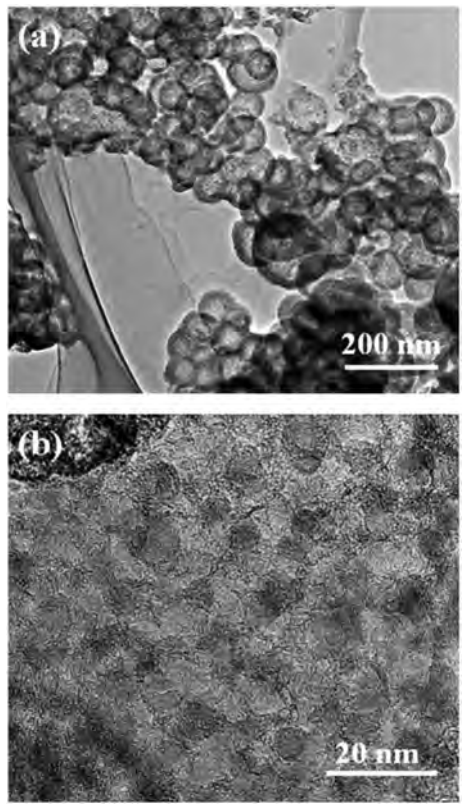

Fig. 7 (a) TEM and (b) HR-TEM images of MSHSs@C/C after 1000 charging/discharging cycles.

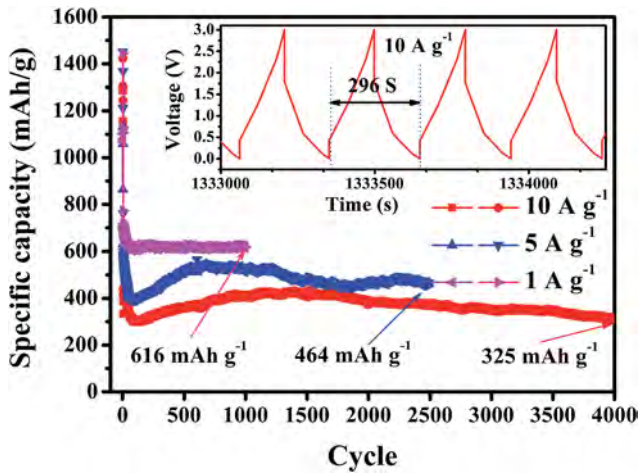

Fig. 6 Long cycling performance of MSHSs@C/C at 1.0, 5.0, and 10.0 A g^{-1} with the inset showing the charging and discharging plots between 3997 and 4000 cycles at a current density of 10.0 A g^{-1}.

Conclusion

MSHSs@C/C was fabricated by double DA polymerization of $MHSnO_2$ and annealing. Ultrasmall Sn nanoparticles (5–8 nm) were uniformly distributed in the shell of the carbon nanosphere and then the Sn/C nanospheres were integrated by the second coating carbon. MSHSs@C/C has a large Sn mass loading of 75%. MSHSs@C/C not only can endure mechanical stress and mitigate pulverization, but also decreases the contact resistance between the spherical particles. The anode made of MSHSs@C/C has a high reversible capacity of 616 mA h g^{-1} at 1.0 A g^{-1} through 1000 cycles as well as outstanding rate and stable performance with a final capacity of 464 mA h g^{-1} at 5.0 A g^{-1} after 2500 cycles and 325 mA h g^{-1} at a larger current density of 10 A g^{-1} up to 4000 cycles. It also has excellent ultrafast rechargeable lithium ion storage ability with a discharging time of less than 2.5 min at a current density of 10.0 A g^{-1}. The robust MSHSs@C/C anode with remarkable comprehensive Li ion storage performance has great potential.

Acknowledgements

This work was financially supported by Natural Science Foundation of China (51504171 and 51572100), Project of Hubei Provincial Education Office (B2015346), Outstanding Young and Middle-aged Scientific Innovation Team of Colleges and Universities of Hubei Province (T201402), Applied Basic Research Program of Wuhan City (2013011801010598) and Project of Natural Science Foundation of Hubei Province (2015CFA116), City University of Hong Kong Applied Research Grant (ARG) No. 9667122.

References

1 M. Armand and J. M. Tarascon, *Nature*, 2008, **451**, 652–657.
2 H. Wu, G. H. Yu, L. J. Pan, N. Liu, M. T. McDowell, Z. N. Bao and Y. Cui, *Nat. Commun.*, 2013, **4**, 1943.
3 Y. X. Tang, Y. Y. Zhang, W. L. Li, B. Ma and X. D. Chen, *Chem. Soc. Rev.*, 2015, **44**, 5926–5940.
4 X. K. Huang, S. M. Cui, J. B. Chang, P. B. Hallac, C. R. Fell, Y. T. Luo, B. Metz, J. W. Jiang, P. T. Hurley and J. H. Chen, *Angew. Chem., Int. Ed.*, 2015, **54**, 1490–1493.
5 M.-H. Park, M. G. Kim, J. Joo, K. Kim, J. Kim, S. Ahn, Y. Cui and J. Cho, *Nano Lett.*, 2009, **9**, 3844–3847.
6 S. L. Jing, H. Jiang, Y. J. Hu, J. H. Shen and C. Z. Li, *Adv. Funct. Mater.*, 2015, **25**, 5395–5401.
7 W. Ni, J. L. Cheng, L. Y. Shi, X. D. Li, B. Wang, Q. Guan, L. Huang, G. F. Gu and H. Li, *J. Mater. Chem. A*, 2014, **2**, 19122–19130.
8 D. H. Youn, A. Heller and C. B. Mullins, *Chem. Mater.*, 2016, **28**, 1343–1347.
9 J. Wang, W. L. Song, Z. Wang, L. Z. Fan and Y. Zhang, *Electrochim. Acta*, 2015, **153**, 468–475.
10 L. W. Ji, Z. Tan, T. Kuykendall, E. J. An, Y. B. Fu, V. Battaglia and Y. G. Zhang, *Energy Environ. Sci.*, 2011, **4**, 3611–3616.
11 Y. J. Zhang, L. Jiang and C. R. Wang, *Nanoscale*, 2015, **7**, 11940–11944.
12 Z. Q. Zhu, S. W. Wang, J. Du, Q. Jin, T. R. Zhang, F. Y. Cheng and J. Chen, *Nano Lett.*, 2014, **14**, 153–157.
13 J. Z. Chen, L. Yang, S. H. Fang, Z. X. Zhang, A. Deb and S.-i. Hirano, *Electrochim. Acta*, 2014, **127**, 390–396.
14 X. Y. Li, Y. M. Chen, H. T. Wang, H. M. Yao, H. T. Huang, Y.-W. Mai, N. Hu and L. M. Zhou, *Adv. Funct. Mater.*, 2016, **26**, 376–383.
15 B. K. Guo, J. Shu, K. Tang, Y. Bai, Z. X. Wang and L. Q. Chen, *J. Power Sources*, 2008, **177**, 205–210.
16 K. Kravchyk, L. Protesescu, M. I. Bodnarchuk, F. Krumeich, M. Yarema, M. Walter, C. Guntlin and M. V. Kovalenko, *J. Am. Chem. Soc.*, 2013, **135**, 4199–4202.
17 B. Luo, T. F. Qiu, L. Hao, B. Wang, M. H. Jin, X. L. Li and L. J. Zhi, *J. Mater. Chem. A*, 2016, **4**, 362–367.
18 M. Wachtler, M. R. Wagner, M. Schmied, M. Winter and J. O. Besenhar, *J. Electroanal. Chem.*, 2001, **510**, 12–19.
19 N. C. Li and C. R. Martin, *J. Electrochem. Soc.*, 2001, **148**, A164–A170.
20 Y. Wang, H. C. Zeng and J. Y. Lee, *Adv. Mater.*, 2006, **18**, 645–649.
21 H. Qiao, Z. Zheng, L. Z. Zhang and L. F. Xiao, *J. Mater. Sci.*, 2008, **43**, 2778–2784.
22 G. Derrien, J. Hassoun, S. Panero and B. Scrosati, *Adv. Mater.*, 2007, **19**, 2336–2340.
23 G. H. Zhang, J. Zhu, W. Zeng, S. H Hou, F. L. Gong, F. Li, C. C. Li and H. G. Duan, *Nano Energy*, 2014, **9**, 61–70.
24 D. H. Youn, A. Heller and B. Mullins, *Chem. Mater.*, 2016, **28**, 1343–1347.
25 X. S. Zhou, J. C. Bao, Z. H. Dai and Y. G. Guo, *J. Phys. Chem. C*, 2013, **11**, 25367–25373.
26 Y. Yu, L. Gu, C. B. Zhu, P. A. Van Aken and J. Maier, *J. Am. Chem. Soc.*, 2009, **131**, 15984–15985.
27 Y. H. Xu, Q. Liu, Y. J. Zhu, Y. H. Liu, A. Langrock, M. R. Zachariah and C. S. Wang, *Nano Lett.*, 2013, **13**, 470–474.
28 I. Meschini, F. Nobili, M. Mancini, R. Marassi, R. Tossici, A. Savoini, M. L. Focarete and F. Croce, *J. Power Sources*, 2013, **226**, 241–248.
29 B. Luo, T. F. Qiu, D. L. Ye, L. Z. Wang and L. J. Zhi, *Nano Energy*, 2016, **22**, 232–240.
30 M. Sha, H. Zhang, Y. T. Nie, K. Q. Nie, X. X. Lv, N. Sun, X. K. Xie, Y. Y. Ma and X. H. Sun, *J. Mater. Chem. A*, 2017, **5**, 6277–6283.
31 X. S. Zhou, L. Yu, X. Y. Yu and X. W. David Lou, *Adv. Energy Mater.*, 2016, **22**, 1601177.
32 K. F. Huo, W. L. An, J. J. Fu, B. Gao, L. Wang, X. Peng, G. J. Cheng and P. K. Chu, *J. Power Sources*, 2016, **324**, 233–238.
33 C. H. Tan, J. Cao, A. M. Khattak, F. P. Cai, B. Jiang, G. Yang and S. Q. Hu, *J. Power Sources*, 2014, **270**, 28–33.
34 F. Paloukis, C. Elmasides, S. G. Neophytidesa and T. Ioannides, *J. Electrochem. Soc.*, 2016, **163**, A1013–A1019.
35 M. Winter and J. O. Besenhard, *Electrochim. Acta*, 1999, **45**, 31–50.
36 Y. Yu, L. Gu, X. Y. Lang, C. B. Zhu, T. Fujita, M. W. Chen and J. Maier, *Adv. Mater.*, 2011, **23**, 2443–2447.
37 V. A. Agubra, L. Zuniga, D. D. L. Garza, L. Gallegos, M. Pokhreland and M. Alcoutlabi, *Solid State Ionics*, 2016, **286**, 72–82.
38 B. Luo, B. Wang, M. H. Liang, J. Ning, X. L. Li and L. J. Zhi, *Adv. Mater.*, 2012, **24**, 1405–1409.
39 Y. Wang, M. H. Wu, Z. Jiao and J. Y. Lee, *Chem. Mater.*, 2016, **21**, 3210–3215.
40 Y. J. Hong and Y. C. Kang, *Small*, 2015, **11**, 2157–2163.
41 K. F. Huo, W. L. An, J. J. Fu, B. Gao, L. Wang, X. Peng, G. J. Gary and P. K. Chu, *J. Power Sources*, 2016, **324**, 233–238.
42 H. B. Wang, C. J. Zhang, Z. H. Liu, L. Wang, P. X. Han, H. X. Xu, K. J. Zhang, S. M. Dong, J. H. Yao and G. L. Cui, *J. Mater. Chem.*, 2011, **21**, 5430–5434.
43 F. C. Zheng, Y. Yang and Q. W. Chen, *Nat. Commun.*, 2014, **5**, 5261.
44 X. M. Jian, J. P. Tu, Y. Q. Qiao, Y. Lu, X. L. Wang and C. D. Gu, *J. Power Sources*, 2013, **236**, 33–38.